

Does the low hole transport mass in 110 and 111 Si nanowires lead to mobility enhancements at high field and stress: A self-consistent tight-binding study

R. Kotlyar, T. D. Linton, R. Rios, M. D. Giles, S. M. Cea et al.

Citation: *J. Appl. Phys.* **111**, 123718 (2012); doi: 10.1063/1.4729806

View online: <http://dx.doi.org/10.1063/1.4729806>

View Table of Contents: <http://jap.aip.org/resource/1/JAPIAU/v111/i12>

Published by the [American Institute of Physics](#).

Related Articles

Influence of catalytic gold and silver metal nanoparticles on structural, optical, and vibrational properties of silicon nanowires synthesized by metal-assisted chemical etching

J. Appl. Phys. **112**, 073509 (2012)

High temperature finite-size effects in the magnetic properties of Ni nanowires

J. Appl. Phys. **112**, 073906 (2012)

Propagation of light in serially coupled plasmonic nanowire dimer: Geometry dependence and polarization control

Appl. Phys. Lett. **101**, 111111 (2012)

On-chip fabrication of ultrasensitive NO₂ sensors based on silicon nanowires

Appl. Phys. Lett. **101**, 103101 (2012)

Morphology and electrical properties of high aspect ratio ZnO nanowires grown by hydrothermal method without repeated batch process

Appl. Phys. Lett. **101**, 083905 (2012)

Additional information on *J. Appl. Phys.*

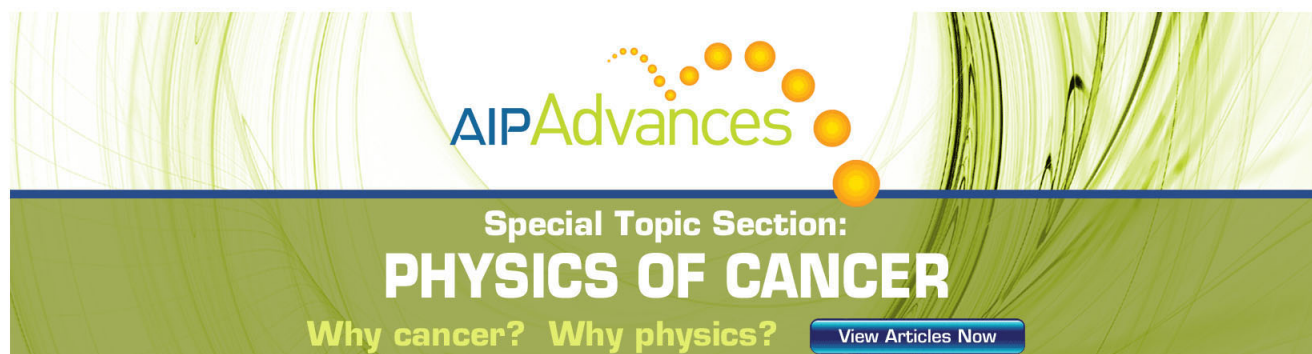
Journal Homepage: <http://jap.aip.org/>

Journal Information: http://jap.aip.org/about/about_the_journal

Top downloads: http://jap.aip.org/features/most_downloaded

Information for Authors: <http://jap.aip.org/authors>

ADVERTISEMENT

The advertisement features a green background with a pattern of thin, wavy lines. At the top, the 'AIP Advances' logo is shown, with 'AIP' in blue and 'Advances' in green, accompanied by a series of orange dots. Below the logo, the text 'Special Topic Section: PHYSICS OF CANCER' is displayed in white, with 'PHYSICS OF CANCER' in a larger, bold font. At the bottom, the phrase 'Why cancer? Why physics?' is written in yellow, and a blue button with the text 'View Articles Now' is positioned on the right.

AIP Advances

Special Topic Section:
PHYSICS OF CANCER

Why cancer? Why physics? [View Articles Now](#)

Does the low hole transport mass in $\langle 110 \rangle$ and $\langle 111 \rangle$ Si nanowires lead to mobility enhancements at high field and stress: A self-consistent tight-binding study

R. Kotlyar,^{1,a)} T. D. Linton,¹ R. Rios,² M. D. Giles,¹ S. M. Cea,¹ K. J. Kuhn,² Michael Povolotskyi,³ Tillmann Kubis,³ and Gerhard Klimeck³

¹Process Technology Modeling, Intel Corporation, 2501 NW 229th Ave., Hillsboro, Oregon 97124, USA

²Component Research, Intel Corporation, 2501 NW 229th Ave., Hillsboro, Oregon 97124, USA

³Network for Computational Nanotechnology, Purdue University, West Lafayette, Indiana 47906, USA

(Received 18 December 2011; accepted 21 May 2012; published online 26 June 2012)

The hole surface roughness and phonon limited mobility in the silicon $\langle 100 \rangle$, $\langle 110 \rangle$, and $\langle 111 \rangle$ square nanowires under the technologically important conditions of applied gate bias and stress are studied with the self-consistent Poisson-sp3d5s*-SO tight-binding bandstructure method. Under an applied gate field, the hole carriers in a wire undergo a volume to surface inversion transition diminishing the positive effects of the high $\langle 110 \rangle$ and $\langle 111 \rangle$ valence band nonparabolicities, which are known to lead to the large gains of the phonon limited mobility at a zero field in narrow wires. Nonetheless, the hole mobility in the unstressed wires down to the 5 nm size remains competitive or shows an enhancement at high gate field over the large wire limit. Down to the studied 3 nm sizes, the hole mobility is degraded by strong surface roughness scattering in $\langle 100 \rangle$ and $\langle 110 \rangle$ wires. The $\langle 111 \rangle$ channels are shown to experience less surface scattering degradation. The physics of the surface roughness scattering dependence on wafer and channel orientations in a wire is discussed. The calculated uniaxial compressive channel stress gains of the hole mobility are found to reduce in the narrow wires and at the high field. This exacerbates the stressed mobility degradation with size. Nonetheless, stress gains of a factor of 2 are obtained for $\langle 110 \rangle$ wires down to 3 nm size at a $5 \times 10^{12} \text{ cm}^{-2}$ hole inversion density per gate area. © 2012 American Institute of Physics. [<http://dx.doi.org/10.1063/1.4729806>]

I. INTRODUCTION

The silicon gate all around (GAA) nanowire is a promising device architecture to achieve ultra short channel devices for continued device density scaling with improved performance.¹ In short channels, ballistic transport is expected where the mean free path of the scattering is comparable to or exceeds the device length. The carrier mean free path is linked to the low field mobility which is a long-channel device characteristic. This important quantity has been subject to significant theoretical attention in silicon wire devices.^{2–7} The electron mobility in cylindrical and square wires for different wire orientations at applied gate fields has been predicted to be reduced in the narrow wires due to the increased electron-phonon and surface roughness scattering.^{2–4,7} Hole mobility studies have been limited to wires at a zero field and no stress.^{5,6} These hole mobility studies point out that the high valence band nonparabolicity leads to large hole mobility gains in narrow $\langle 110 \rangle$, and $\langle 111 \rangle$ wires only limited by phonon scattering. The experimental measurements of hole mobility range from the reported peak mobility values of $1350 \text{ cm}^2/\text{Vs}$ in 10–20 nm diameter back-gated cylindrical wires⁸ to significantly below the universal planar limit mobility in square $4 \times 5 \text{ nm}^2$ $\langle 110 \rangle$ wires.⁹ To explain the experiments, we present a theoretical study of hole mobility under the technologically important conditions of an applied gate

field and an applied stress. In particular, we address the question if the high nonparabolicity gains in the narrow wires extend to high fields and stresses and yield a high hole mobility under normal operating conditions in devices.

II. METHOD

We consider infinitely long square undoped silicon nanowires and surrounded by 1 nm of oxide gated on all sides. The three important wire channel orientations $\langle 100 \rangle$, $\langle 110 \rangle$, and $\langle 111 \rangle$ are studied. The side surface wafer orientations for the simulated wires are (100) ($\langle 100 \rangle$) and (110) ($\langle 110 \rangle$ and $\langle 111 \rangle$). The bandstructures of the Si wires are calculated using the sp3d5s*-SO 20-orbital tight-binding model implemented in the NEMO5 simulator.^{10,13} The surface states are passivated using the sp3 hybridization approach.¹¹ A uniform strain modifies the wire unit cell. Strain is included in the Hamiltonian by modifying the overlap integrals due to a bond stretching and including the diagonal shifts due to strain as described in Ref. 12 with Boykin *et al.*'s tight-binding parameter set.¹⁴ For the same-atom diagonal shifts, the same-orbital stress corrections are included. The presence of an oxide and an applied gate voltage affects the bandstructure of the wire through the included self-consistent Hartree potential, obtained by solving the three dimensional Poisson equation in a wire unit cell and a tight-binding bandstructure iteratively using a Nonlinear Poisson convergence scheme.¹⁵ Gate bias is modeled as a Dirichlet boundary condition for the electric potential. In each iteration, the equilibrium quantum

^{a)}Author to whom correspondence should be addressed. E-mail: roza.kotlyar@intel.com.

density is constructed from the calculated bandstructure, and this density is used by the Poisson equation in the next iteration. A Krylov-Schur projection method eigensolver is used to obtain the eigenvalues of the tight-binding Hamiltonian in each self-consistent iteration.¹⁵ In each iteration, we provide to the eigensolver a value of the top subband energy from a previous iteration as a shift parameter around which to calculate the desired eigenspectrum (i.e., valence bands in this case). With this eigensolver “guidance” method, we achieve the self-consistent solution typically within 10–15 iterations. This method allows us to “focus” the eigensolver on the appropriate interval of the desired spectrum in the presence of the strong band bending under high gate fields. We simulate square wires in the range of 3×3 to 15×15 nm². We also simulated a rectangular 10×35 nm² wire gated on the top and the two sides for the comparison with the planar limit at the high field. We include up to 100 valence subbands in the self-consistent bandstructure and scattering calculations. The hole momentum relaxation rates and the mobility for the included acoustic and optical phonon scattering, and the surface roughness scattering processes are calculated as a postprocessing step after achieving convergence of the Schrödinger-Poisson equations solution. The models used for the scattering calculations are described below, and in the included Appendices.

We take the wire channel orientation as the x-direction, y-z as the cross-section plane. The position \vec{r}_{jl} of the l th atom in a wire of N_x unit cells is specified by the position \vec{R}_j of the j th unit cell and a coordinate \vec{r}_l of the atom within this cell

$$\vec{r}_{jl} = \vec{R}_j + \vec{r}_l. \quad (1)$$

Both the number of the atomic layers normal to x in a wire unit cell and the unit cell lattice constant width a_x depend on the wire orientation, but do not depend on the wire cross-section size. For example, a $\langle 100 \rangle$ wire has 4 (y-z) planar atomic layers in a three-dimensional wire unit cell. The carrier wavefunction for a subband n with a quasi-momentum k_x along the wire within the tight-binding approach is given by

$$\begin{aligned} \psi_{k_x}^n(x, y, z) &= \frac{1}{\sqrt{N_x}} \sum_{jlm} C_{ml}^n(k_x) e^{ik_x \cdot x_{jl}} \cdot \phi_{ml}(\vec{r} - \vec{r}_{jl}) \equiv |nk_x\rangle \\ &\equiv \frac{1}{\sqrt{N_x}} \sum_j \tilde{\psi}_{k_x j}^n e^{ik_x \cdot x_j} \equiv \frac{1}{\sqrt{N_x}} \sum_j e^{ik_x \cdot x_j} |\widetilde{nk_x j}\rangle. \end{aligned} \quad (2)$$

In Eq. (2), the orthonormal Löwdin atomic functions¹⁶ ϕ_{ml} ($\vec{r} - \vec{r}_{jl}$) for the m th orbital of an atom at \vec{r}_{jl} contain all the dimensionality of the global wavefunction $|nk_x\rangle$. The tight-binding expansion coefficients $C_{ml}^n(k_x)$ are unitless. The extent of the atomic functions determines an atom “size” (or an atomic volume V_{atom}).¹⁷ In Eq. (2), the second line includes various definitions which we introduce and re-use below.

Using the orthonormality of the atomic functions, we construct for the Poisson equation the integrated hole charge density around each atom position

$$\int_l d^3r \rho_h(r) = e \sum_n \int a_x \frac{dk_x}{2\pi} \sum_m C_{ml}^{n*}(k_x) C_{ml}^n(k_x) f^n(k_x), \quad (3)$$

where $f^n(k_x)$ is the Fermi-Dirac equilibrium distribution function evaluated at the subband energy $E_n(k_x)$.

We include the scattering of holes in a wire with the bulk silicon acoustic and optical phonons. The confinement of the acoustic phonons is expected to have only a minor impact on our results for the studied wire sizes of 3 to 15 nm.⁵ The momentum-relaxation rate $\Gamma_{nn'}(k_x)$ for the hole phonon deformation potential scattering from an initial subband n to a final subband n' is calculated using the relaxation time approximation (RTA) and is given by

$$\begin{aligned} \Gamma_{nn'}(k_x) &= \frac{2\pi}{\hbar} \sum_{q, q_y, q_z, k'_x} |\langle nk_x | U(\vec{q}) | n'k'_x \rangle|^2 \left(1 - \frac{k'_x}{k_x}\right) \\ &\times \frac{1 - f(E')}{1 - f(E)} \delta(E' - E \mp \hbar\omega\vec{q}). \end{aligned} \quad (4)$$

In Eq. (4), \vec{q} and $\omega\vec{q}$ are the bulk phonon momenta and frequency dispersion, respectively. The \mp in the energy conserving delta-function correspond to the phonon absorption and phonon emission processes. $U(\vec{q})$ describes the hole-phonon interaction Hamiltonian. Using this approach and the approximations described in the Appendix A, Eq. (4) is evaluated as

$$\Gamma_{nn'}^{ac}(k_x) = \frac{2\pi}{\hbar} \int \frac{dk'_x}{2\pi} \left[\Sigma_{ac}^2 \frac{kT}{\rho v_s^2} \right] F_{nk_x, n'k'_x} \delta(E' - E). \quad (5)$$

Similarly, for the hole-optical phonon scattering, we obtain

$$\begin{aligned} \Gamma_{nn'}^{opt}(k_x) &= \frac{2\pi}{\hbar} \int \frac{dk'_x}{2\pi} \left[\Xi_{opt}^2 \frac{\hbar}{2\rho\omega_0} \left(n_0 + \frac{1}{2} \mp \frac{1}{2} \right) \right] \\ &\times \frac{1 - f(E')}{1 - f(E)} F_{nk_x, n'k'_x} \delta(E' - E \mp \hbar\omega_0). \end{aligned} \quad (6)$$

The tight-binding bandstructure is solved on a uniform tensor grid in half of k-space for no stress and for uniaxial stresses. The uniform grid consists of 100 k_x points in $[0, 0.3] 2\pi/a_x$. The integration over k-grid includes $\pm k_x$ using the time-reversal symmetry of the bandstructure. Eigenvalues are computed at each (k_x) grid point, but the computationally expensive hole-phonon overlaps $F_{nk_x, n'k'_x}$ in Eqs. (5) and (6) are computed on a 1/5 sparser k-grid and then interpolated for the entire k-grid. A similar k-grid approach to the computation of the hole-phonon overlap integrals for hole phonon scattering in confined surface channels can be found in Ref. 17.

We include the surface scattering of holes at each of the four surfaces of a rough wire, assuming that the roughness values $\Delta_i(x)$ ($i = 1, 2, 3, 4$) on different surfaces are uncorrelated. We consider the roughness $\Delta_i(x)$ which arises from the shift of one of the surfaces as a whole: at the cell position x in a wire a layer (or layers) of atoms along one of the wire cross-section dimensions (y or z) is added to or subtracted from the wire cross-section unit cell. Fourier analysis of the general roughness function shows that a rigid shift normal to the surface gives the largest contribution to the surface roughness.³ The momentum-relaxation rate for the surface roughness scattering on a single surface i is given by

$$\Gamma_{nn'}^i(k_x) = \frac{2\pi}{\hbar} \sum_{k'_x} |\langle nk_x | V_{SR}^i | n'k'_x \rangle|^2 \left(1 - \frac{k'_x}{k_x}\right) \delta(E' - E). \quad (7)$$

Keeping only the terms linear in roughness, the interaction potential is written as $V_{SR}^i \equiv \tilde{V}_{SR}^i \Delta_i(x)$. We use the approximations of an unscreened surface roughness potential and include the Prange-Nee term.¹⁸ Generalizing the results of Refs. 3 and 4 to the tight-binding model, we write the matrix element as

$$V_{SRnk_x, n'k'_x}^i = \langle nk_x | \left[\frac{\partial H}{\partial r_c} \Big|_{V=const} + \frac{\partial V}{\partial r_c} (1 - |r_c^i - r_c|/t_i) + (E_n - E_{n'}) (1 - |r_c^i - r_c|/t_i) \frac{\partial}{\partial r_c} \right] \Delta_i(x) | n'k'_x \rangle, \quad (8)$$

r_c is the coordinate of the wire dimension of length t_i normal to the rough surface: for the top and the bottom surfaces $r_c = z$, for the left and the right surfaces $r_c = y$. r_c^i are the corresponding coordinates of these surfaces. E_n and $E_{n'}$ are the subband energies. V is the electrostatic potential energy. Using this approach and the approximations described in the Appendix B, the hole-surface roughness momentum relaxation rate in a wire is evaluated as

$$\Gamma_{nn'}^i(k_x) = \frac{2\pi}{\hbar} \int \frac{dk'_x}{2\pi} \left(1 - \frac{k'_x}{k_x}\right) |F_{n0n'0}^i|^2 \langle \Delta_{iq_{x\pm}}^2 \rangle \delta(E' - E). \quad (9)$$

The hole surface roughness overlap $F_{n0n'0}^i$ has dimensions of energy/length and is evaluated using Eq. (B4). The average roughness $\langle \Delta_{iq_{x\pm}}^2 \rangle$ with $q_{x\pm} = k'_x \pm k_x$ is calculated using the correlation function with a correlation length λ and a RMS roughness Δ given in Eq. (B3).

All included scattering rates are summed, and the result is inverted to obtain the total momentum relaxation time $\tau_x^n(k_x)$ which is used to calculate the low field hole mobility along the wire for each subband n

$$\mu_{xx}^n = \frac{e}{\hbar n_h^n} \int \frac{dk_x}{2\pi} v_x^n(k_x) \tau_x^n(k_x) \frac{\partial f^n(k_x)}{\partial k_x}, \quad (10)$$

n_h^n is the hole density in a subband, and $v_x^n(k_x) = \frac{1}{\hbar} \frac{\partial E}{\partial k_x}$ is the hole velocity in a subband n at k_x , respectively. The total hole mobility is obtained by summing over the subbands $n \mu_{xx} = \sum_n n_h^n \mu_{xx}^n / n_h$, where n_h is the total hole density summed over all subbands. To study the effects of the band-structure modifications under an applied field and external stress independent from the scattering rate changes, we compute the inverse transport mass as

$$\left(\frac{1}{m}\right)_{xx}^n = \frac{1}{\hbar n_h^n} \int \frac{dk_x}{2\pi} v_x^n(k_x) \frac{\partial f^n(k_x)}{\partial k_x}. \quad (11)$$

We also compute the injection velocity in the ballistic limit in the top of the barrier model¹⁹

$$v_x^n = \frac{\int \frac{dk_{x+}}{2\pi} v_x^n(k_{x+}) f^n(k_{x+})}{\int \frac{dk_{x+}}{2\pi} f^n(k_{x+})}. \quad (12)$$

The equilibrium Fermi energy for the velocity calculation is computed using the density of the carriers moving with $+k_x$ only.

III. RESULTS AND DISCUSSION

Narrow $\langle 110 \rangle$ and $\langle 111 \rangle$ wires have a high valence band nonparabolicity which gives light transport mass and high phonon mobility at zero gate field. This result has been highlighted in earlier work.^{5,6} We obtain a similar dependence of the phonon mobility computed at zero applied gate field and at a low linear hole density of $1 \times 10^4 \text{ cm}^{-1}$ as a function of the wire size shown in Fig. 1. We use the parameters $\Sigma_{ac} = 5.6 \text{ eV}$, $\Xi_{opt} = 13.24 \times 10^8 \text{ eV/cm}$, $\hbar\omega_0 = 61.2 \text{ meV}$ (Ref. 23) in Eqs. (5) and (6). Our acoustic potential value is close to the value of 5.39 eV used in Ref. 6. The changes in the band nonparabolicity as a function of the wire size are directly reflected in the enhancements ($\langle 110 \rangle$, $\langle 111 \rangle$) or near-invariance ($\langle 100 \rangle$) of the inverse transport mass in Fig. 1. Note that the phonon scattering in narrow structures is increased for all the wire orientations. The increased phonon scattering comes from the large hole-phonon overlaps $F_{nk_x, n'k'_x}$ in Eqs. (5) and (6) due to the strong hole geometry size confinement in narrow wires. The calculated hole-phonon overlaps in narrow wires increase over their values in the larger simulated $15 \times 15 \text{ nm}^2$ size wires. The corresponding ratios of the subband population averaged phonon-hole overlaps in the reference $\langle 110 \rangle 15 \times 15 \text{ nm}^2$ size wire to their values in the $l_x \times l_y \text{ nm}^2$ size wire, $|\langle F_{nk_x, n'k'_x}^{(110)}(15 \times 15) \rangle| / |\langle F_{nk_x, n'k'_x}(l_x \times l_y) \rangle|$, reduce in wires down to $3 \times 3 \text{ nm}^2$ sizes in Fig. 1. In Eq. (1), when the shown normalized

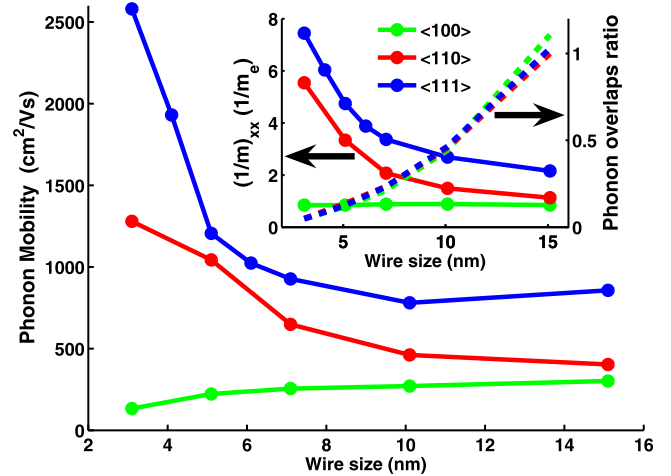


FIG. 1. The phonon-limited mobility, the inverse transport mass (in the inset lines with symbols), and the ratio of the subband population averaged phonon-hole overlaps $|\langle F_{nk_x, n'k'_x}^{(110)}(15 \times 15) \rangle| / |\langle F_{nk_x, n'k'_x}(l_x \times l_y) \rangle|$ (in the inset lines with dashes) as a function of square nanowire size $l_x = l_y$ for the $\langle 100 \rangle$, $\langle 110 \rangle$, and $\langle 111 \rangle$ transport channels computed at a zero gate field and at a low fixed hole inversion linear density of $1 \times 10^4 \text{ cm}^{-2}$. Due to the strong geometry size confinement in narrow wires, the hole-phonon overlaps increase from their values in the larger simulated $15 \times 15 \text{ nm}^2$ size wires and the corresponding hole-phonon overlap ratios reduce in wires down to $3 \times 3 \text{ nm}^2$ sizes. The increase of the band curvature along the $\langle 110 \rangle$ and $\langle 111 \rangle$ directions leads to inverse transport mass and mobility enhancements at small wire sizes. For $\langle 100 \rangle$ channels, the inverse transport mass is nearly flat and the phonon-limited mobility is dominated by the geometry size confinement degradation in the narrow wires.

ratios are less than 1, the phonon scattering is stronger in a wire than it is in the reference wide wire. Therefore, size effects on the mass and size effects on the phonon scattering compete. This leads to smaller gains for 3 nm over 15 nm wires in the phonon mobility of factors of 3.2 and 3.0 as compared to these gains in the inverse transport mass of factors of 4.9 and 3.4 in $\langle 110 \rangle$ and $\langle 111 \rangle$ channels, respectively. With the inverse transport mass being near flat as a function of the wire size, we obtain a degradation of the phonon mobility by a factor of 2.3 in $\langle 100 \rangle$ 3 nm wire. Note that the effect of the band nonparabolicity on the inverse transport mass diminishes at 15 nm in $\langle 110 \rangle$ wires. For these wire sizes, the phonon mobility approaches the bulk hole mobility in silicon. In contrast, in $\langle 111 \rangle$ wires, the inverse transport mass is twice the values of $\langle 110 \rangle$ and $\langle 100 \rangle$ wires, and the mobility is high at 15 nm wire size.

The gains in the inverse transport mass and the phonon-limited mobility obtained in the $\langle 110 \rangle$ and $\langle 111 \rangle$ narrow wires due to the high nonparabolicity at a zero field diminish greatly at the high fields. The gate field enables a transition from volume inversion (low field or low inversion density) to surface inversion (high field or high inversion density). It is of technological importance to compute hole mobility under p-channel Metal Oxide Semiconductor Field Effect Transistor (PMOSFET) operating conditions in devices in the range of $5 \times 10^{12} - 1 \times 10^{13} \text{ cm}^{-2}$ carrier density per gate area. The evolution of the carrier density distribution as a function of the applied gate field in $5 \times 5 \text{ nm}^2$ and $15 \times 15 \text{ nm}^2$ wires shown in Fig. 2 progresses from volume inversion at low fields to the surface inversion at high fields. This transition occurs at lower fields in larger structures. The bands show a strong bending at the silicon/oxide interface at high fields. The band curvature, and consequently, the

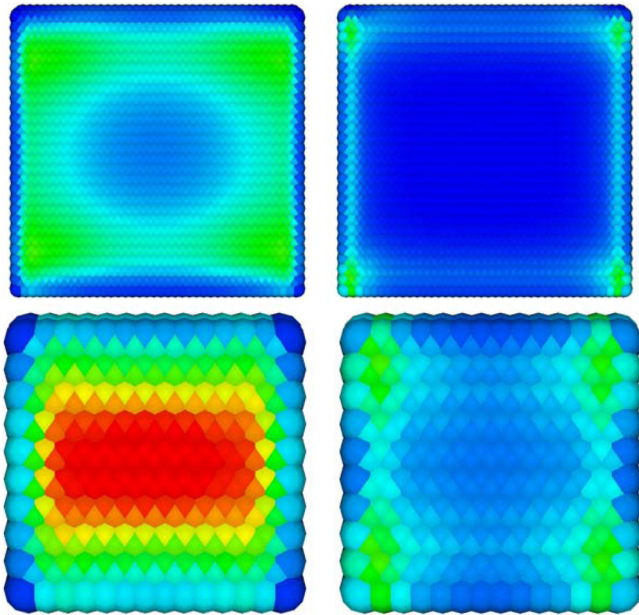


FIG. 2. A volume to surface hole inversion transition in $\langle 110 \rangle$ wires is shown as a function of the $l_y \times l_z \text{ nm}^2$ wire size and the applied gate field: 15×15 at $1.6 \times 10^{12} \text{ cm}^{-2}$ (top left), 15×15 at $1.4 \times 10^{13} \text{ cm}^{-2}$ (top right), 5×5 at $1.2 \times 10^{12} \text{ cm}^{-2}$ (bottom left), and 5×5 at $1.5 \times 10^{13} \text{ cm}^{-2}$ (bottom right). The hole charge distributions (Eq. (3)) in the wire atomic unit cells are shown.²⁵ The color scale is from blue to red $10^{-6} - 3 \times 10^{-4}$ (left), $10^{-4} - 10^{-2}$ (right) in e units.

inverse transport mass, the phonon limited mobility, and the hole-phonon overlaps which are shown in Figs. 3(a)–3(c) evolve as a function of the applied field due to this transition. In the shown range of hole densities, the inverse transport masses reduce from their zero gate field values by factors of 1.8 and 1.6 in the $\langle 110 \rangle$ and $\langle 111 \rangle$ 3 nm wires, respectively. The corresponding reductions in the phonon-limited mobility by factors of 4.2 and 6.1 are amplified by the increased scattering due to a strong field-induced confinement. The ratios of the subband population averaged phonon-hole overlaps in the reference $\langle 110 \rangle$ $15 \times 15 \text{ nm}^2$ size wire at 0 field to their values in the $l_x \times l_y \text{ nm}^2$ size wire, $|\langle F_{nk_x, nk_y}^{(110), 0 \text{ field}}(15 \times 15) \rangle| / |\langle F_{nk_x, nk_y}(l_x \times l_y) \rangle|$, reduce at high field in Fig. 3(c). In Fig. 3(c), when the shown normalized ratios are less than 1, the phonon scattering is stronger in a wire than it is in the reference wide wire. In the larger $10 \times 10 \text{ nm}^2$ and $15 \times 15 \text{ nm}^2$ $\langle 110 \rangle$ and the $10 \times 10 \text{ nm}^2$ $\langle 111 \rangle$ wires, the inverse transport mass improves at high field. The phonon limited mobility peaks at low densities due to the competing lower mass and stronger scattering effects in these larger crosssection wires. At high inversion densities, the field confinement leads to a lower mobility in the $10 \times 10 \text{ nm}^2$ than in $3 \times 3 \text{ nm}^2$ $\langle 100 \rangle$ wires which have the inverse transport mass and the hole-phonon overlaps weakly dependent on the field. The inter-subband hole-phonon scattering contributes to the mobility degradation in the $10 \times 10 \text{ nm}^2$ $\langle 100 \rangle$ wire at the high field where the lowest subband spacing is much lower than the thermal energy kT , whereas it is minimal in the $3 \times 3 \text{ nm}^2$ $\langle 100 \rangle$ wire where the lowest subband spacing varies from 0.9 to 1.3 kT in the shown range of fields in Fig. 3.

We validate our surface roughness model with the planar device limit. In Fig. 4, we compare our simulated phonon and surface roughness limited mobility in the $10 \times 35 \text{ nm}^2$ $\langle 110 \rangle$ and $\langle 100 \rangle$ rectangular wires gated on the top and the two sides with planar $\langle 110 \rangle$ channel PMOSFET data at high field for the $\langle 100 \rangle$ and $\langle 110 \rangle$ wafer orientations.²⁰ At high inversion density in the surface inversion regime, the $\langle 110 \rangle$ wire mobility is dominated by the $\langle 110 \rangle$ side surfaces and it approaches the $\langle 110 \rangle / \langle 110 \rangle$ planar data values. Similarly, at high field, the $\langle 100 \rangle$ wire mobility approaches the $\langle 110 \rangle / \langle 100 \rangle$ planar data values. This agreement validates our simulations because $\langle 100 \rangle$ and $\langle 110 \rangle$ channels have the same hole mobility in the planar limit on a $\langle 100 \rangle$ wafer. The surface roughness parameters are $\lambda = 3.0 \text{ nm}$ and $\Delta = 0.65 \text{ nm}$, which are similar to the values used by us in the modeling of hole surface channel mobility.¹⁸ A detailed comparison with experiments is not available at present due to a large scatter in the wire data and the presence of additional charge sources of degradation, which are not included in our model.^{8,9}

Surface roughness scattering dominates in small wires at low gate bias. Hole mobility degradation due to surface roughness scattering depends on the hole mass along the normal of the rough surface. In Figs. 5(a)–5(c), we show the evolution of the wire size dependence of phonon and surface roughness limited mobility as a function of the field strength. For $\langle 110 \rangle$ and $\langle 111 \rangle$ channels with a high phonon limited mobility, the total mobility is dominated by surface roughness scattering at low fields in the small size wires.⁷ It reduces mobility by factors of about 20 ($\langle 110 \rangle$), 3.4 ($\langle 111 \rangle$),

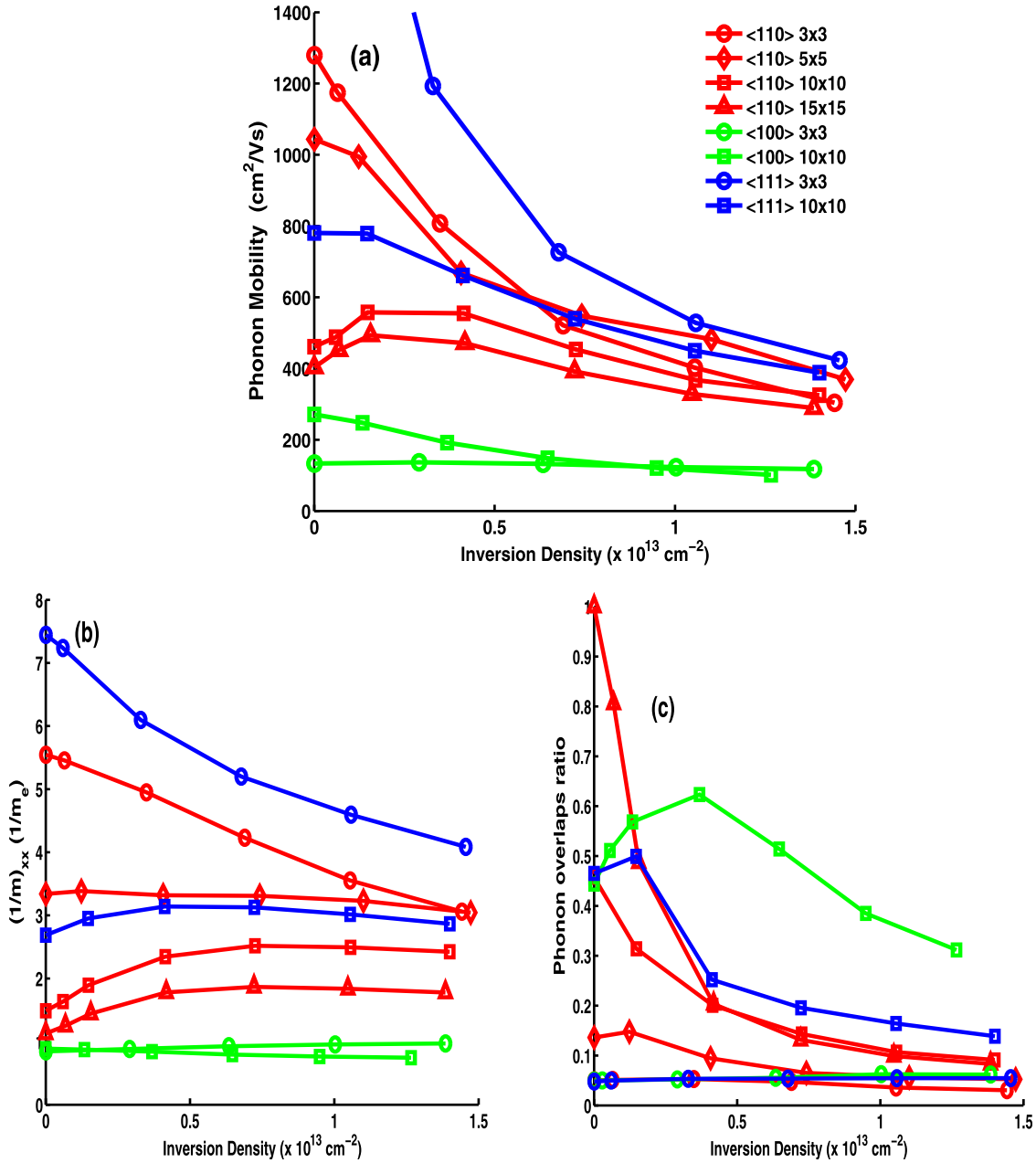


FIG. 3. The phonon limited mobility (a), the inverse transport mass (b), and the ratio of the subband population averaged phonon-hole overlaps $|\langle F_{n0n0}^{(110),0 \text{ field}}(15 \times 15) \rangle| / |\langle F_{n0n0}^i(lx \times ly) \rangle|$ (c) as a function of the hole inversion areal density (linear density/gated perimeter). The wire sizes $lx \times ly$ and the channel orientations are given in the legend. After the onset of surface inversion, the nonparabolicity gains of the small $\langle 110 \rangle$ and $\langle 111 \rangle$ wires diminish, and the mobility decreases due to the strong field confinement.

and by a smaller factor of 1.6 ($\langle 100 \rangle$) in the 3 nm wires. The strength of the surface roughness scattering in the wire depends on the wafer orientation of the rough atomic surface. This effect is more pronounced at smaller cross-section sizes. The degradation of the surface roughness limited mobility in the narrow wires comes from the strong size dependence of F_{n0n0}^i in Eq. (9). We calculate the subband population averaged surface roughness overlap $\langle F_{n0n0}^i \rangle$ for each surface, and find that $\langle F_{n0n0}^{(100)} \rangle \gg \langle F_{n0n0}^{(110)} \rangle, \langle F_{n0n0}^{(11-2)} \rangle$ in narrow wires. We show the ratios of the subband population averaged surface roughness overlap in the reference $\langle 110 \rangle 15 \times 15 \text{ nm}^2$ size wire at 0 field for the surface roughness scattering with the (110) surface to their values in the $lx \times ly \text{ nm}^2$

size wire, $|\langle F_{n0n0}^{(110)/(110),0 \text{ field}}(15 \times 15) \rangle|^2 / |\langle F_{n0n0}^i(lx \times ly) \rangle|^2$, as a function of wire size in Figure 5(d). In Figure 5(d), when the shown normalized ratios are less than 1, the surface roughness scattering is stronger in a wire than it is in the reference wide wire. For example, at zero field in a 3 nm $\langle 110 \rangle$ wire the scattering with the top and bottom (100) surfaces is much stronger than the scattering with the side (110) surfaces with the ratio of the corresponding average overlaps of a factor of 9. This result can be understood from a simple particle-in-a-box picture. The dependence of the kinetic energy in the first term in Eq. (8) on the wire size predominantly determines the magnitude of the surface roughness scattering at low field. This dependence is inversely proportional to the

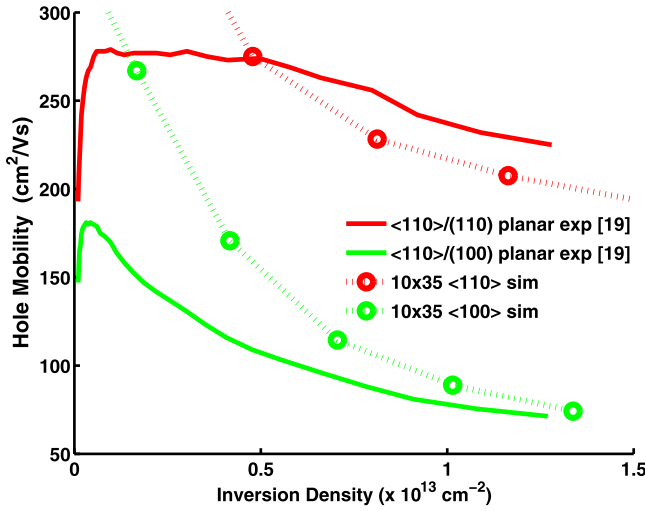


FIG. 4. The phonon and surface roughness limited mobility in 10×35 $\langle 100 \rangle$ and $\langle 110 \rangle$ wires gated on the top and the two sides simulated as a function of the areal hole density is compared with the experimental $\langle 110 \rangle$ planar surface channel mobility on $\langle 110 \rangle$ and $\langle 100 \rangle$ wafers.²⁰

carrier mass along the direction normal to the surface. For $\langle 110 \rangle$ surfaces this mass is heavy, while for $\langle 100 \rangle$ surfaces it is light. This confinement mass asymmetry leads, for

example, to the carrier inversion on the $\langle 110 \rangle$ surfaces first at a finite field in Eq. (2). The $\langle 110 \rangle$ wires have two strong surface scattering surfaces (top and bottom) in contrast to the $\langle 111 \rangle$ wire that experiences a weaker scattering. Therefore, the reduction of the hole mobility due to surface roughness scattering is stronger in the $\langle 110 \rangle$ than in the $\langle 111 \rangle$ wires. The strength of the surface roughness scattering in the wire also depends on the wire channel orientation. The dependence of the surface overlaps on the wire channel orientation comes from the strong coupling of the x and y degrees of freedom in the tight-binding Hamiltonian, and from the corresponding anisotropic valence bandstructure in the wire cross-section plane. The subband population averaged surface overlap for $\langle 100 \rangle$ side surfaces is larger for $\langle 110 \rangle$ wire than it is in the $\langle 100 \rangle$ wire at zero field shown in Figure 5(d).

At intermediate (corresponding to $5 \times 10^{12} \text{ cm}^{-2}$ density) and at high field (corresponding to $1 \times 10^{13} \text{ cm}^{-2}$ density), both the phonon and surface-roughness limited mobilities are reduced due to a strong surface field confinement. The surface overlaps at the high field in wires down to 5 nm size increase over their values in the reference $\langle 110 \rangle 15 \times 15 \text{ nm}^2$ size wire at 0 field in Figure 5(d). At a high inversion density and larger crosssections, the second and the third terms in Eq. (8) give the largest contributions to

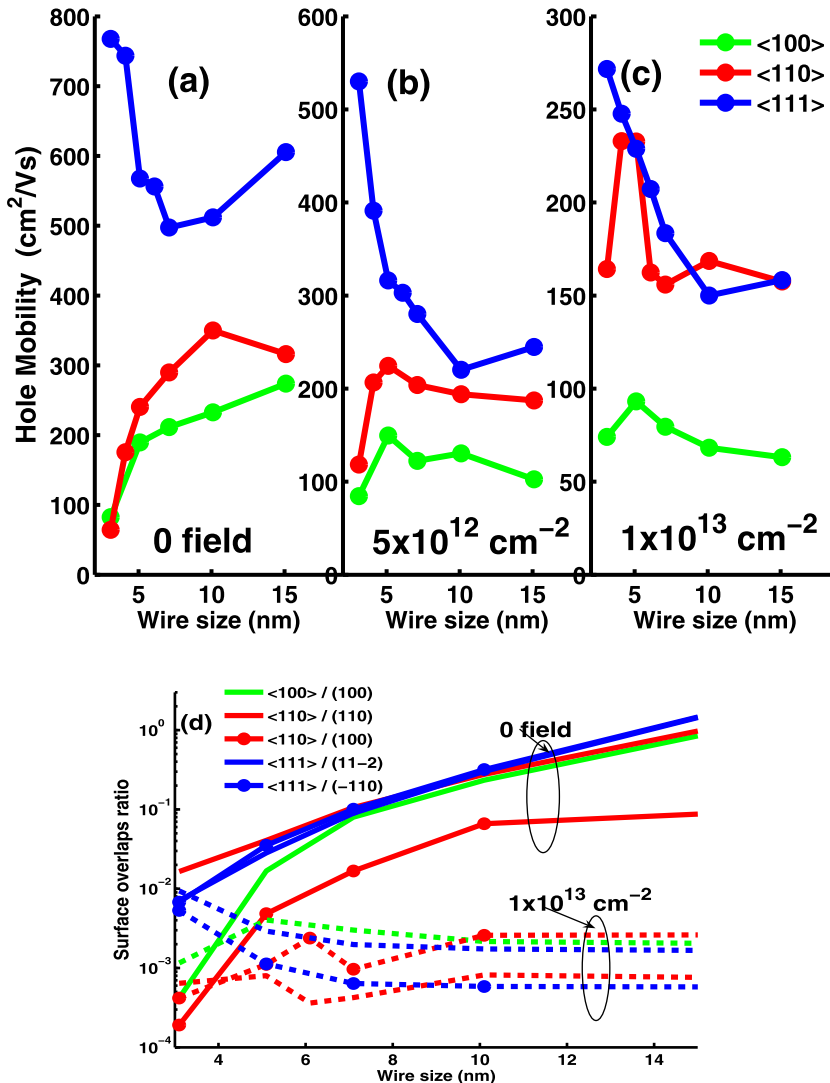


FIG. 5. The wire size dependence evolution of the hole mobility in $\langle 100 \rangle$, $\langle 110 \rangle$, and $\langle 111 \rangle$ channels as a function of the field: at a zero field (a), at $5 \times 10^{12} \text{ cm}^{-2}$ (b), $1 \times 10^{13} \text{ cm}^{-2}$ (c). The ratio of the subband population averaged surface-roughness overlaps $|\langle F_{n0n0}^{(110)/(\langle 110 \rangle, 0 \text{ field})} (15 \times 15) \rangle|^2 / |\langle F_{n0n0}^{(\text{channel})/(\text{surface})} (Lx \times Ly) \rangle|^2$ (d) as a function of square nanowire size $Lx = Ly$ computed at a zero gate field (solid) and at $1 \times 10^{13} \text{ cm}^{-2}$ (dashes). The channel and the surface orientations for the surface overlaps are given in the legend. Surface roughness is the dominant scattering mechanism at the high field and at the small wire size. In the $\langle 100 \rangle$ and $\langle 110 \rangle$ wires, it is responsible for the mobility reduction in the narrow wires at the low field. At high fields under strong field confinement, the hole mobility shows an enhancement due to the volume inversion at the 4–5 nm $\langle 100 \rangle$ and $\langle 110 \rangle$ wire sizes. The surface roughness scattering depends on the orientation of the transport channel and on the orientation of the transport surface.

surface roughness. In the self-consistent tight-binding bandstructure-Poisson solution, the different confinement masses along normals to wire surfaces lead to the hole carrier distribution peaks being closer to the (110) surface than to the (100) surface in the $\langle 110 \rangle$ wire in Eq. (2). The corresponding surface overlaps for the (100) surfaces are smaller than their values for the (110) surfaces in the $\langle 110 \rangle$ wires down to 5 nm size shown in Figure 5(d) at the high field. Note this trend in the overlap dependence on the rough surface orientation at high field in larger wires is reversed from the zero field limit where the first kinetic energy term in Eq. (8) gives the largest contributions to the surface roughness scattering in narrow wires. In the intermediate and the high field regime, the total mobility in both the $\langle 100 \rangle$ and the $\langle 110 \rangle$ wires shows a peak at 4–5 nm sizes and it is increasing in down from 10 nm size $\langle 111 \rangle$ wires due to less surface scattering as carriers re-distribute away from the silicon/oxide interfaces under volume inversion. The $\langle 111 \rangle$ wires lose their hole mobility advantage over the $\langle 110 \rangle$ wires at high field and wire sizes larger than 10 nm. The corresponding surface overlaps in the $\langle 111 \rangle$ wires are larger than their values in the $\langle 110 \rangle$ wires at high field and wire sizes larger than 10 nm in Figure 5(d).

Stress warps the valence bands and increases the non-parabolicity along the $\langle 110 \rangle$ and $\langle 111 \rangle$ directions enhancing hole mobility. At a low gate bias, strain effects are larger in larger wires. We study hole mobility in wires under an applied compressive longitudinal uniaxial channel stress. Such stress has been a reliable booster of the device performance in PMOSFET devices for several technology generations.²¹ We show the stress responses of the hole mobility and the inverse transport mass for 3, 5, 7, and 10 nm $\langle 110 \rangle$ wires at $5 \times 10^{12} \text{ cm}^{-2}$ in Fig. 6(a). We take the applied stress to be uniform in a wire and convert this stress to strain using a bulk silicon compliance tensor. We use the resultant strain tensor to construct the strained wire lattice unit cell, modify the tight-binding Hamiltonian by the strain, and perform self-consistent calculations as we have discussed in Sec. II. The stress warps the valence bands and enhances the nonparabolicity along the $\langle 110 \rangle$ direction. This enhancement is reduced for the narrow wire bands that have high band curvatures due to the geometry size confinement. The inverse transport mass stress gains reduce in the narrow wires, achieving a factor of 1.6 in the 3 nm wire in Fig. 6(a). We note that under a 1D confinement or 2D transport, the warping due to stress causes the repopulation of carriers in 2D k-space to the regions perpendicular to the transport and stress direction for $\langle 110 \rangle / \langle 100 \rangle$ surface channels.¹⁸ In a wire, where the k-space is 1D, the repopulation effect due to the warping does not occur. Stress affects the hole mobility through the stress induced changes of the transport mass, the confinement masses in the wire cross-section, the subband splitting, and band mixing. At a low field (not shown in the figure), the hole mobility has progressively larger responses for the larger structures, varying from a factor of 1.6 for a 3 nm wire to a factor of 5 for a 10 nm wire under -3 GPa stress. This is largely driven by the transport mass gains with stress. At $5 \times 10^{12} \text{ cm}^{-2}$, the same trend is obtained in the wires starting from the 5 nm size.

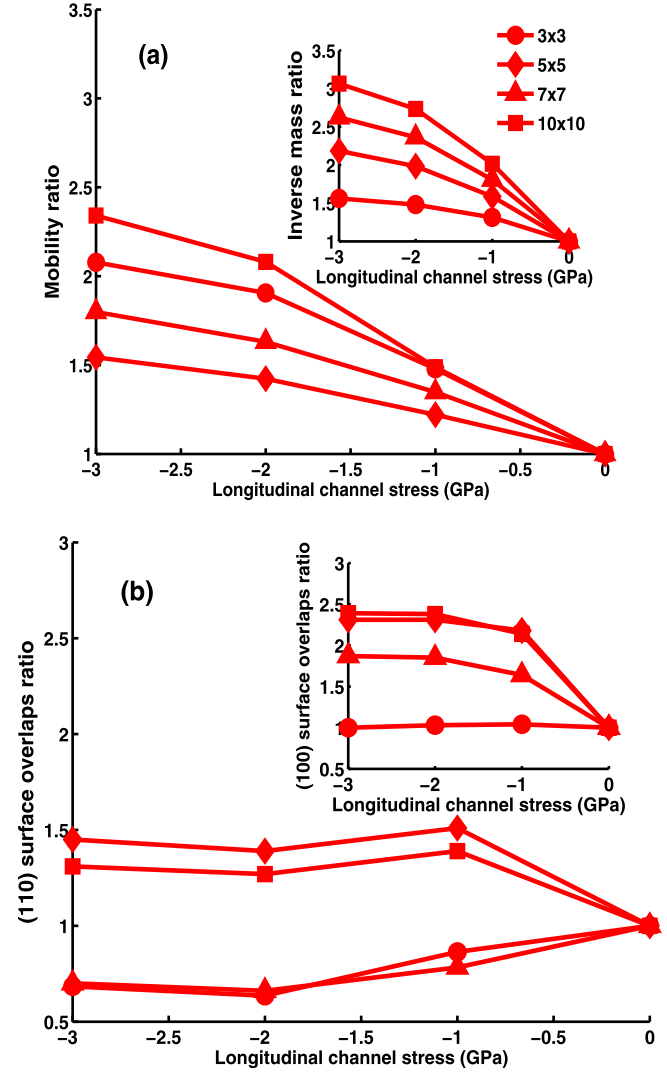


FIG. 6. (a) The ratio of the mobility and the inverse transport mass (inset) and (b) the ratio of the subband population averaged surface roughness overlaps $|\langle F_{n0m0}^i \rangle|^2$ under stress to their unstressed values for $\langle 110 \rangle$ wires as a function of stress. Results in (b) are shown for i for the right (110) and the top (100) (inset) surfaces. Mobility gains under an applied compressive longitudinal uniaxial channel stress are obtained for all the 3, 5, 7, and 10 nm wire sizes simulated at $5 \times 10^{12} \text{ cm}^{-2}$.

The effect of increased surface roughness scattering overlap with stress competes with inverse transport mass gains reducing stress gains of the hole mobility. This overlap, as discussed above, depends on the confinement masses in a wire cross-section plane. Its changes with stress are different for the (100) and (110) surfaces as shown in Fig. 6(b). For $\langle 110 \rangle$ compressive stress, the y-mass increases with stress and z-mass decreases with stress in a wire. The average overlap and surface scattering for the (110) surface decrease in the 3 nm wires with stress. For the (100) surface, they are enhanced with stress. This enhancement reduces in small geometries where the stress induced confinement mass changes saturate. As a result, the 3 nm wire has larger stress gains than the 5 nm wire for which the surface roughness scattering is enhanced with stress.

Stress effect gains are modulated by volume to surface inversion transition as a function of applied gate field, and

are lowered at high fields. The size dependence of the hole mobility under an applied -2 GPa compressive longitudinal stress in the $\langle 100 \rangle$, $\langle 110 \rangle$, and $\langle 111 \rangle$ wires as a function of field is studied in Figs. 7(a)–7(c). At a vanishingly small field, for all the studied channel orientations the stress gains reduce at the smaller sizes. This exacerbates the mobility degradation with wire size. The stress gains reduce with the strength of the confinement field in Figs. 7(b) and 7(c). At $1 \times 10^{13} \text{ cm}^{-2}$ in $4\text{--}5 \text{ nm}$ $\langle 110 \rangle$ wires, stress leads to degradation of mobility due to the increased surface scattering overlaps. We show the ratios of the subband population averaged surface roughness overlap in the reference $\langle 110 \rangle 15 \times 15 \text{ nm}^2$ size unstressed wire at 0 field for the surface roughness scattering for the $\langle 110 \rangle$ surface to their values in the $l_x \times l_y \text{ nm}^2$ size wire under -2 GPa compressive longitudinal stress, $|\langle F_{n0n0}^{(110)/(110),0\text{field}}(15 \times 15) \rangle|^2 / |\langle F_{n0n0}^{(i)}(l_x \times l_y) \rangle|^2$, as a function of wire size in Figure 7(d). In Figure 7(d), when the shown normalized ratios are less than 1, the surface roughness scattering is stronger in a wire than it is in the reference unstressed wide wire. Note the overall larger surface roughness overlaps in the stressed case in Figure 7(d) as compared to the unstressed overlaps shown in Figure 5(d).

Mobility enhancement due to the transition to the volume inversion regime is obtained for the $\langle 100 \rangle$ 5 nm wire. In the narrow $\langle 111 \rangle$ wires, the surface roughness scattering is weaker than in the $\langle 100 \rangle$ and $\langle 110 \rangle$ wires as we have discussed earlier. This also be seen in smaller overlaps in the $\langle 111 \rangle$ wires than in the $\langle 100 \rangle$ and $\langle 110 \rangle$ stressed wires at 3 nm size in Figure 7(d). The $\langle 111 \rangle$ wires also have smaller stress gains than the $\langle 110 \rangle$ channels. As in the no stress case, with the transition to surface inversion at high density, the $\langle 111 \rangle$ wires lose their advantage under strong field confinement for sizes larger than 10 nm .

In a ballistic limit, only mass changes under geometry and field confinement matter. In this limit, in ultra-scaled gate length devices, scattering is expected to play less of a role in transport. We show the injection velocity calculated in this limit as a function of wire size, channel orientation and stress at a $5 \times 10^{12} \text{ cm}^{-2}$ inversion density in Fig. 8. The velocity is enhanced in the narrow $\langle 110 \rangle$ and $\langle 111 \rangle$ wires and it is further enhanced by an applied -2 GPa uniaxial channel stress. The advantage of the $\langle 111 \rangle$ over $\langle 110 \rangle$ narrow wires is modest with no stress and it is lost under the applied stress.

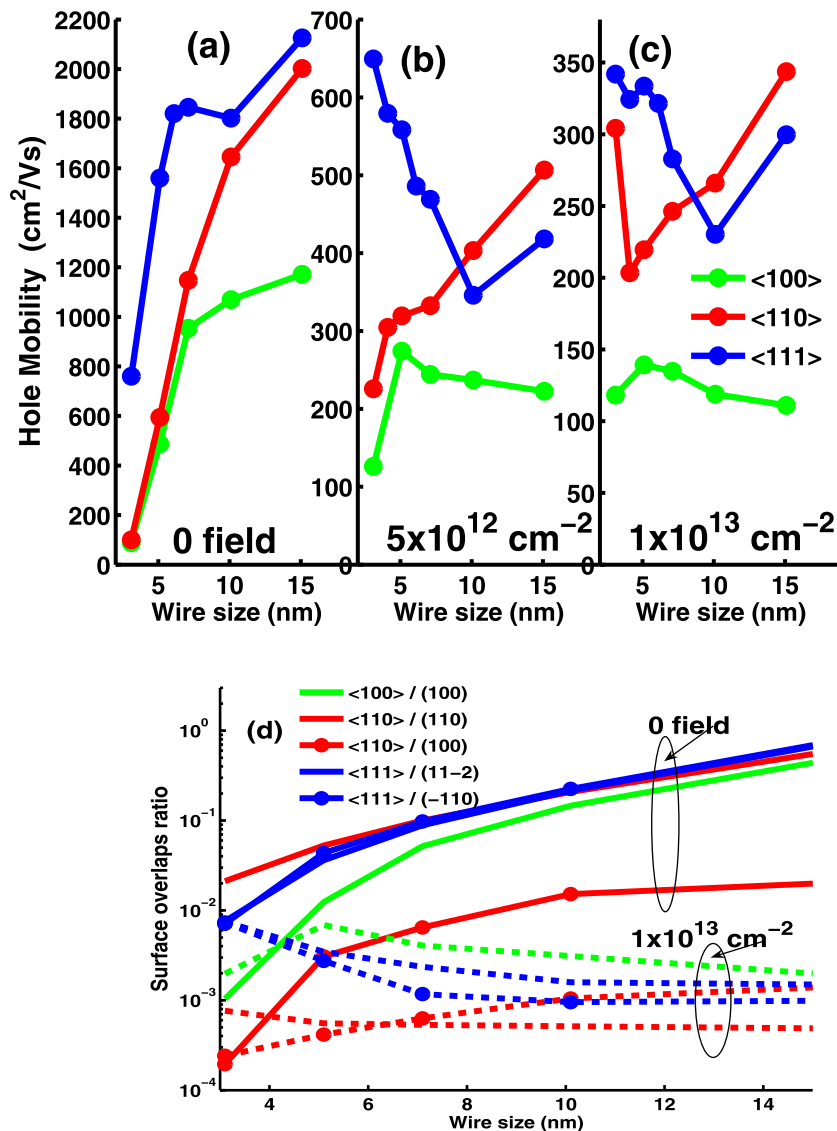


FIG. 7. The wire size dependence evolution of hole mobility in $\langle 100 \rangle$, $\langle 110 \rangle$, and $\langle 111 \rangle$ channels under an applied -2 GPa compressive longitudinal uniaxial channel stress as a function of field: at a zero field (a), at $5 \times 10^{12} \text{ cm}^{-2}$ (b), $1 \times 10^{13} \text{ cm}^{-2}$ (c). The ratio of the subband population averaged surface-roughness overlaps $|\langle F_{n0n0}^{(110)/(110),0\text{field},0\text{stress}}(15 \times 15) \rangle|^2 / |\langle F_{n0n0}^{(channel)/(surface)}(l_x \times l_y) \rangle|^2$ (d) as a function of square nanowire size $l_x = l_y$ computed at a zero gate field (solid) and at $1 \times 10^{13} \text{ cm}^{-2}$ (dashes). The channel and the surface orientations for the surface overlaps are given in the legend. The mobility stress gains reduce for the smaller wires and at the higher fields.

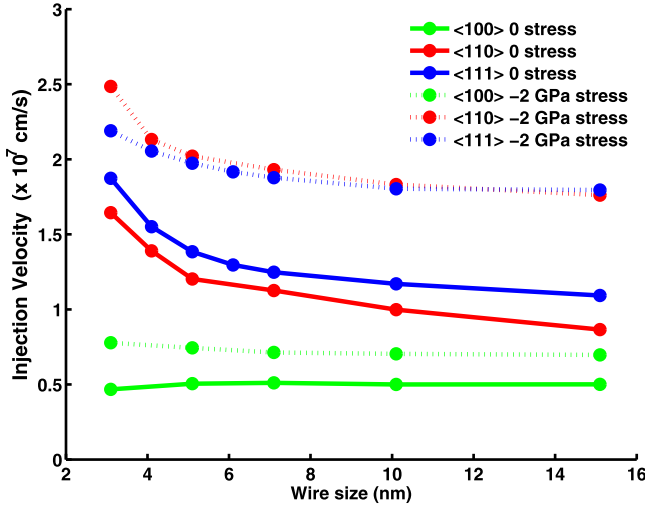


FIG. 8. The injection velocity unstressed (solid lines) and under an applied -2 GPa compressive longitudinal uniaxial channel stress (dotted) as a function of the wire size simulated at $5 \times 10^{12} \text{ cm}^{-2}$ inversion density. In the ballistic limit only band nonparabolicity matters, and the velocity is enhanced in the narrow wires and by the applied stress.

IV. CONCLUSIONS

The self-consistent tight-binding theoretical study of hole mobility in square silicon nanowires for sizes ranging from 3 to 15 nm, for the three important wire channel orientations $\langle 100 \rangle$, $\langle 110 \rangle$, and $\langle 111 \rangle$, and for a range of applied gate fields and applied stresses is presented. The scattering with bulk silicon acoustic and optical phonons is included within a tight-binding model and the calculated hole phonon limited mobility is compared with the Si bulk mobility limit in large wires. An inverse transport mass in wires is calculated to elucidate the bandstructure effects independent from the scattering changes as a function of field and stress. It is found that the high valence band nonparabolicities diminish at high field, reducing the phonon limited mobility advantage of the narrow $\langle 110 \rangle$ and $\langle 111 \rangle$ wires. A realistic model for the surface scattering due to roughness of each wire surface is considered, and is compared to the planar mobility in the high field limit. The physics of the surface roughness scattering for different wafer orientations of the rough surfaces in a wire is elucidated. It is found that the $\langle 110 \rangle$ and $\langle 11-2 \rangle$ orientations experience less surface roughness scattering than the $\langle 100 \rangle$ surfaces. For $\langle 111 \rangle$ wires, in conjunction with the high valence band nonparabolicity, this leads to a high hole mobility in up to 10 nm wire sizes and up to intermediate fields at a $5 \times 10^{12} \text{ cm}^{-2}$ hole inversion density per gate area. A compressive channel stress along the wire direction is shown to lead to mobility gains for all studied orientations. The stress gains are found to reduce in narrow wires. Still, stress gains of a factor of 2 are obtained for $\langle 110 \rangle$ wires down to 3 nm size at a $5 \times 10^{12} \text{ cm}^{-2}$ hole inversion density per gate area. It is shown that in the ballistic limit at this inversion density gains of a factor of 1.8 are obtained for the injection velocity of the 3 nm $\langle 110 \rangle$ wire. The $\langle 111 \rangle$ wires lose their advantage to the $\langle 110 \rangle$ wires under an applied stress in this limit. Our results show that the $\langle 110 \rangle$ wire hole mobility remains competitive to the hole planar mobility at high field and high stress, making wires an attractive

PMOSFET candidate for continued device scaling. Finally, we note that our results present theoretical expectations as a guide for hole mobility over wide experimental conditions to help understand the large scatter seen in hole mobility wire data.

ACKNOWLEDGMENTS

The authors would like to thank Portland Technology Development and Components Research at Intel for joint collaboration in this work. R. Kotlyar also would like to thank Dr. D. Nikonov for the early discussions on the selection of the bandstructure codes for this work. The supercomputer Redsky at the Sandia National Lab and an internal Intel High Power Computing Cluster were used for the computations of our results presented in this paper. Work at Purdue University was supported by NSF PetaApps grant number OCI-0749140, the Semiconductor Research Corporation's (SRC) Nanoelectronics Research Initiative (NRI) and National Institute of Standards & Technology through the Midwest Institute for Nanoelectronics Discovery (MIND), and the MSD Focus Center, one of six research centers funded under the Focus Center Research Program (FCRP).

APPENDIX A: HOLE-PHONON SCATTERING

We start with the expression in Eq. (4). The interaction Hamiltonian $U(\vec{r})$ arises from the changes in the crystal potential V due to ionic vibrations in the phonon modes $\omega(\vec{q})$ and is given by $\vec{\Delta}V \cdot \vec{u}(\vec{r})$. The bulk ionic displacement field $\vec{u}(\vec{r})$ is given by⁴

$$\vec{u}(\vec{r}) \equiv \sum_{\vec{q}} \vec{u}_{\vec{q}} = \sum_{\vec{q}} \sqrt{\frac{\hbar}{2\rho V \omega_{\vec{q}}}} (a_{\vec{q}} e^{i\vec{q} \cdot \vec{r}} + h.c.) e_{\vec{q}}, \quad (\text{A1})$$

where ρ , V , and $e_{\vec{q}}$ are the crystal density, volume, and the polarization vector, respectively. $a_{\vec{q}}$ ($a_{\vec{q}}^\dagger$) are the phonon annihilation (creation) operators. The displacement field of the acoustic mode describes the in-phase motion of the atoms in a bulk unit cell. The Fourier transform of the interaction potential with the acoustic mode is $U(\vec{q}) \equiv U_+(\vec{q}) + U_-(\vec{q})$, where

$$U_{\pm}^{ac}(\vec{q}) = \pm i \Sigma_{ac}(e_{\vec{q}} \cdot \vec{q}) \sqrt{\frac{\hbar}{2\rho V \omega_{\vec{q}}}} \left(n_{\vec{q}} + \frac{1}{2} \mp \frac{1}{2} \right)^{1/2} e^{\pm i\vec{q} \cdot \vec{r}} \\ \equiv \tilde{U}_{\pm}^{ac}(\vec{q}) e^{\pm i\vec{q} \cdot \vec{r}}. \quad (\text{A2})$$

Equation (A2) is obtained by evaluating the expectation value of the interaction potential between the initial and final states of the phonon bath with an equilibrium phonon occupation, given by the Bose-Einstein statistics

$$n_{\vec{q}} = \left(\frac{\hbar \omega_{\vec{q}}}{e^{kT}} - 1 \right)^{-1}. \quad (\text{A3})$$

The displacement field of the optical mode describes the out-of-phase motion of the two atoms in a silicon bulk unit cell. Using the same definitions as in Eq. (A2), we write the interaction potential with the optical mode as

$$U_{\pm}^{opt}(\vec{q}) = \Xi_{opt} \sqrt{\frac{\hbar}{2\rho V \omega_{\vec{q}}}} \left(n_{\vec{q}} + \frac{1}{2} \mp \frac{1}{2} \right)^{1/2} e^{\pm i\vec{q} \cdot \vec{r}} \\ \equiv \tilde{U}_{\pm}^{opt}(\vec{q}) e^{\pm i q_x x}, \quad (\text{A4})$$

Σ_{ac} and Ξ_{opt} are the acoustic and optical deformation potentials. In the matrix element in Eq. (4) for each interaction potential $U_{\pm}^p(\vec{q})$ (p = an acoustic or an optical process) the integration over the wire of length L_x is broken in the integration over the unit cell and the sum over unit cells

$$\langle nk_x | U_{\pm}^p(\vec{q}) | n'k'_x \rangle = \langle \widetilde{nk_x} | \tilde{U}_{\pm}^p(\vec{q}) | \widetilde{n'k'_x} \rangle \sum_j \frac{e^{i(k'_x \pm q_x - k_x) \cdot x_j}}{N_x} \\ = \langle \widetilde{nk_x} | \tilde{U}_{\pm}^p(\vec{q}) | \widetilde{n'k'_x} \rangle \frac{2\pi \delta_{k'_x \pm q_x - k_x, K_x}}{L_x}. \quad (\text{A5})$$

The sum over wire unit cells in Eq. (A5) gives the conservation of the momenta along the wire within the reciprocal lattice vector K_x of a wire. Similarly as in bulk,²² we take the terms $e^{i(k'_x - k_x) \cdot x_j} \approx 1$ over the small width of the wire unit cell. The summation over phonon momenta converted to integration in Eq. (4) and using Eq. (A5) gives

$$\sum_{q_x, q_y, q_z} |\langle nk_x | U_{\pm}^p(\vec{q}) | n'k'_x \rangle|^2 \\ = V \int \int \int \frac{dq_x}{2\pi} \frac{dq_y}{2\pi} \frac{dq_z}{2\pi} |\langle nk_x | U_{\pm}^p(\vec{q}) | n'k'_x \rangle|^2 \\ = \frac{|\langle U_{\pm}^p(0) \rangle|^2}{L_x} \int d^3r \int d^3r' \tilde{\psi}_{k_x}^{n*}(x, y, z) \tilde{\psi}_{k'_x}^{n'}(x, y, z) \tilde{\psi}_{k_x}^n \\ \times (x', y', z') \tilde{\psi}_{k'_x}^{n'*}(x', y', z') \times \int \int \frac{dq_y}{2\pi} \frac{dq_z}{2\pi} e^{iq_y(y-y')} e^{iq_z(z-z')}. \quad (\text{A6})$$

We used the isotropic and equipartition approximation employed previously by us and elsewhere to the hole acoustic scattering in the confined channels

$$|\langle U_{\pm}^{ac}(0) \rangle|^2 = \Sigma_{ac}^2 \frac{kT}{2\rho v_s^2}, \quad (\text{A7})$$

where v_s is the average sound velocity.^{18,23} For the optical phonon scattering, considering one branch of the frequency ω_0 we get

$$|\langle U_{\pm}^{opt}(0) \rangle|^2 = \Xi_{opt}^2 \frac{\hbar}{2\rho \omega_0} \left(n_0 + \frac{1}{2} \mp \frac{1}{2} \right). \quad (\text{A8})$$

The last double integral in Eq. (A6) gives a product of $\delta(y - y')$ $\delta(z - z')$ and this equation simplifies to

$$\frac{|\langle U_{\pm}^p(0) \rangle|^2}{L_x} \int d^3r \int d^3r' \tilde{\psi}_{k_x}^{n*}(x, y, z) \tilde{\psi}_{k'_x}^{n'}(x, y, z) \tilde{\psi}_{k_x}^n \\ \times (x', y, z) \tilde{\psi}_{k'_x}^{n'*}(x', y, z) \equiv \frac{|\langle U_{\pm}^p(0) \rangle|^2}{L_x} F_{nk_x n'k'_x}. \quad (\text{A9})$$

The last expression defines the hole-phonon scattering overlap integral $F_{nk_x n'k'_x}$ in the tight-binding model.

The hole-phonon scattering overlap integral $F_{nk_x n'k'_x}$ has the dimensions of 1/area. Its evaluation involves computing the integrals over the atomic wavefunctions:

$$F_{nk_x n'k'_x} = \sum_{l_1 m_1 l_2 m_2 l_3 m_3 l_4 m_4} C_{m_1 l_1}^{n*}(k_x) C_{m_2 l_2}^{n'}(k'_x) C_{m_3 l_3}^n(k_x) \\ \times C_{m_4 l_4}^{n'*}(k'_x) \int d^3r \int d^3r' \phi_{m_1 l_1}^*(\vec{r} - \vec{r}_{l_1}) \phi_{m_2 l_2}(\vec{r} - \vec{r}_{l_2}) \\ \times \phi_{m_3 l_3}(\vec{r}' - \vec{r}_{l_3}) \phi_{m_4 l_4}^*(\vec{r}' - \vec{r}_{l_4}), \quad (\text{A10})$$

where $\vec{r} = (x, y, z)$ and $\vec{r}' = (x', y, z)$. Using the orthonormality of the Löwdin atomic functions for computational efficiency, we approximate the hole-phonon scattering overlap as

$$F_{nk_x n'k'_x} = \sum_{lm} C_{ml}^{n*}(k_x) C_{ml}^{n'}(k'_x) C_{ml}^n(k_x) C_{ml}^{n'*}(k'_x) \frac{a_x}{4V_{atom}}, \quad (\text{A11})$$

where $V_{atom} = 4\pi R^3/3$ with R taken as the Slater atomic radius for silicon of 1.15 Å.¹⁷ The factor of 4 in Eq. (A11) arises assuming an exponential radial decay of the four atomic functions in Eq. (A10). The integral over x' gives the factor of a_x . In the final evaluation, we approximate $F_{nk_x n'k'_x} \approx F_{nk_x n'k'_x}$. Combining all the results and changing from a summation over the final momentum k'_x to the integration $\int \frac{L_x dk'_x}{2\pi}$ in Eq. (4), we obtain Eqs. (5) and (6). Our computed phonon mobility for the larger size $\langle 110 \rangle$ wires approaches the Si bulk phonon mobility value in Eq. (1) showing that our approximations in the calculations of the hole-phonon overlaps give a reasonable accuracy of our results.

APPENDIX B: HOLE-SURFACE ROUGHNESS SCATTERING

$\Delta_i(x)$ in Eq. (8) is expanded in the Fourier series:

$$\Delta_i(x) = \sum_{q_{x\pm}} \Delta_{iq_{x\pm}} e^{\pm i q_{x\pm} x}. \quad (\text{B1})$$

Similar to the phonon case, the integration over the wire is broken into integration over the wire unit cell and summation over the unit cells. The last summation gives the conservation of the momenta along the wire within the reciprocal lattice vector K_x of a wire in a surface scattering process. We obtain for the squared matrix element

$$|\langle nk_x | V_{SR}^i | n'k'_x \rangle|^2 = |\langle \widetilde{nk_x} | \tilde{V}_{SR}^i | \widetilde{n'k'_x} \rangle|^2 \langle \Delta_{iq_{x\pm}}^2 \rangle, \quad (\text{B2})$$

where $q_{x\pm} = k'_x \pm k_x$. We compute the averaged surface roughness using the correlation function $\langle \Delta(0)\Delta(x) \rangle = \Delta^2(x\sqrt{2}/\lambda)^n K_n(x\sqrt{2}/\lambda)$, where K_n is a modified Bessel function of the third kind, λ is the correlation length, and Δ is the rms fluctuation of the surface. We use $n = 2$.^{18,23} Taking the Fourier transform of this correlation function, we obtain for the roughness power spectrum in a wire²⁴

$$S(q_{x\pm}) = \langle \Delta_{iq_{x\pm}}^2 \rangle = \frac{3\pi \Delta^2 \lambda}{4 L_x} \frac{1}{(1 + q_{x\pm}^2 \lambda^2/2)^{2.5}}. \quad (\text{B3})$$

Since $S(q_{x\pm})$ is a rapidly decaying function at large q_x , we evaluate the matrix element in Eq. (B1) between $k_x = k'_x = 0$ states.

The matrix element in Eq. (8) consists of the three terms. $\frac{\partial H}{\partial r_c}|_{V=\text{const}}$ describes the change of the kinetic energy with the change of wire crosssection. It does not depend on the carrier distribution and therefore it is not expected to depend strongly on the applied gate field.⁴ We evaluate this term at zero electrostatic potential as $\frac{\partial E_n}{\partial r_c}|_{V=0}$ for the intra-subband transitions. We compute the subband energies E_n^0 and E_n of a wire of the original size, and of a wire with one atomic layer added in a unit cell to the considered rough surface. Then $\frac{\partial E_n}{\partial r_c}|_{V=0} \approx (E_n - E_n^0)/dr_c$ with dr_c equal to the increase in the wire crosssection dimension normal to the surface. The other two terms in Eq. (8) depend on the applied field and we evaluate these terms by computing the spatial derivatives on a finite element mesh. The integrals over the atomic functions we approximate using their orthonormality property. We obtain for the surface roughness overlap

$$F_{n0n'0}^i = \frac{\partial E_n}{\partial r_c}|_{V=0} \delta_{n,n'} + \sum_{lm} C_{ml}^{n*} C_{ml}^{n'} \frac{\partial V}{\partial r_c} \bigg|_l (1 - |r_c^i - r_{lc}|/t_i) + (E_n - E_{n'}) \sum_{lm} C_{ml}^{n*} \frac{\partial C_{ml}^{n'}}{\partial r_c} (1 - |r_c^i - r_{lc}|/t_i), \quad (\text{B4})$$

$\frac{\partial V}{\partial r_c}|_l$ and $\frac{\partial C_{ml}^{n'}}{\partial r_c}$ are evaluated by interpolating the potential and the wavefunction for each orbital component m between the atom positions and the finite element mesh nodes. These derivatives are then evaluated on the finite element mesh and

the results are interpolated back at the atom positions. Combining all the results and doing the integration over the final momentum k'_x , we obtain Eq. (9).

- ¹N. Singh *et al.*, Tech. Dig. -Int. Electron Devices Meet. **2006**, 1.
- ²R. Kotlyar *et al.*, *Appl. Phys. Lett.* **84**, 5270 (2004).
- ³S. Jin *et al.*, *J. Appl. Phys.* **102**, 083715 (2007).
- ⁴I. Ramayya *et al.*, *J. Appl. Phys.* **104**, 063711 (2008).
- ⁵A. K. Buin *et al.*, *Nano Lett.* **8**, 760 (2008).
- ⁶N. Neophytou *et al.*, *Nano Lett.* **10**, 493 (2010).
- ⁷S. G. Kim *et al.*, *IEEE Trans. Electron Devices* **58**, 1371 (2011).
- ⁸Y. Cui *et al.*, *Nano Lett.* **3**, 149 (2003).
- ⁹J. Chen *et al.*, *VLSI* **2010**, 175.
- ¹⁰S. Steiger *et al.*, in *Device Research Conference*, 2011.
- ¹¹S. Lee *et al.*, *Phys. Rev. B* **69**, 045316 (2004).
- ¹²T. B. Boykin *et al.*, *Phys. Rev. B* **76**, 035310 (2007).
- ¹³G. Klimeck *et al.*, *CMES* **3**, 601 (2002).
- ¹⁴T. B. Boykin *et al.*, *Phys. Rev. B* **69**, 115201 (2004).
- ¹⁵NEMO5 simulator manual, Network for Computational Nanotechnology, Purdue University, 2011. The eigensolver “guidance” method described here has been included as one of simulation options in the NEMO5 manual.
- ¹⁶P. O. Löwdin, *J. Chem. Phys.* **18**, 365 (1950).
- ¹⁷J. C. Slater, *Phys. Rev.* **36**, 57 (1930).
- ¹⁸R. Kotlyar *et al.*, *J. Comput. Electron.* **8**, 110 (2009).
- ¹⁹M. S. Lundstrom and J. Guo, *Nanoscale Transistors: Device Physics, Modeling and Simulation* (Springer, 2006).
- ²⁰H. Irie *et al.*, Tech. Dig. -Int. Electron Devices Meet. **2004**, 225.
- ²¹T. Ghani *et al.*, Tech. Dig. -Int. Electron Devices Meet. **2003**, 978.
- ²²J. Singh, *Electronic and Optoelectronic Properties of Semiconductor Structures* (Cambridge University Press, 2003).
- ²³M. V. Fischetti *et al.*, *J. Appl. Phys.* **94**, 1079 (2003).
- ²⁴For the evaluation of this integral, we used the formula (3.371) from the I. S. Gradshteyn and I. M. Ryzhik, *Tables of Integrals, Sums, Progressions and Products* (State Publishing of Physics-Mathematics Literature, Moscow, 1963).
- ²⁵See <https://wci.llnl.gov/codes/visit/>, for information on the visualization software, Lawrence Livermore National Laboratory, 2011.